ECS Transactions, 64 (38) 13-30 (2015)
10.1149/06438.0013ecst ©The Electrochemical Society

Graphitic Carbon Nitride Materials for Energy Applications

A. Belen Jorge[a], I. Dedigama[a], N. Mansor[a], R. Jervis[a], T. S. Miller[b], F. Corà[b], P. Shearing[a], C. Gibbs[a], P. F. McMillan[b], and D. J. L Brett[a]

[a] Electrochemical Innovation Lab, University College London, London WC1E 7JE, UK
[b] Department of Chemistry, University College London, London WC1H 0AJ, UK

Polymeric layered carbon nitrides were investigated for use as catalyst support materials for proton exchange membrane fuel cells (PEMFCs) and water electrolyzers (PEMWEs). Three different carbon nitride materials were prepared: a heptazine-based graphitic carbon nitride material (gCNM), poly (triazine) imide carbon nitride intercalated with LiCl component ($PTI-Li^+Cl^-$) and boron-doped graphitic carbon nitride (B-gCNM). Following accelerated corrosion testing, all graphitic carbon nitride materials were found to be more electrochemically stable compared to conventional carbon black (Vulcan XC-72R) with B-gCNM support showing the best stability. For the supported Pt, $Pt/PTI-Li^+Cl^-$ exhibited the best durability with only 19% electrochemical surface area (ECSA) loss versus 36% for Pt/Vulcan. Superior methanol oxidation activity was observed for all gCNM supported Pt catalysts on the basis of the catalyst ECSA. Preliminary results on IrO_2 supported on gCNM using a PEMWE cell revealed an enhancement in the charge-transfer resistance as the current density increases when compared to unsupported IrO_2. This may be attributed to a higher active surface area of the catalyst nanoparticles on the gCNM support.

Introduction

Polymeric carbon nitrides first discovered in the late 19th century (1,2) are $C_xN_yH_z$ compounds with a high N:C ratio that are attracting new interest due to their unique and useful properties for applications ranging from electronic charge storage to redox catalysis and photocatalysis (3-17). The structures are based on triazine (C_3N_3) or heptazine (C_6N_7) ring units linked by -N= or -NH- bridges to form sheets or zigzag chains of monomer units linked by hydrogen bonds to give a 2D array. Examples include Liebig's melon, melem, or other highly condensed $C_xN_yH_z$ polymeric structures formed by continued elimination of NH_3 component, eventually leading to graphitic sheets (Figure 1). Recent discussions are mainly based on polymerized heptazine models that are more thermodynamically stable following extended sheet condensation, but other structures containing s-triazine ring elements can also be produced under different synthesis conditions and both structure types may be present within the nanocrystalline materials. The materials are semiconducting with an intrinsic bandgap near 2.7 eV and optical absorption extending into the visible range that can be associated with the bandgap or localized transitions (12).

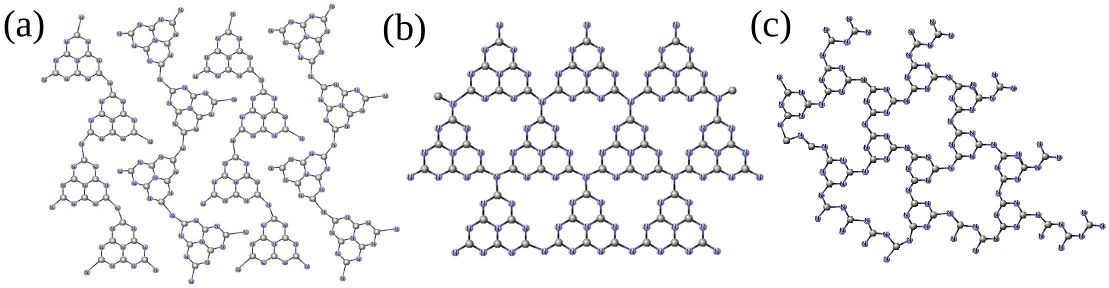

Figure 1. (a)The structure of Liebig's melon ($[C_6N_7(NH_2)(NH)]_n$). Zig-zag chains of heptazine (tri-*s*-triazine) units are linked by bridging -NH- groups and decorated on their edges by N-H groups, (b) fully condensed graphitic carbon nitride structure based on heptazine block units, and (c) fully condensed gCNM based on triazine ring units.

Because of their high nitrogen content, tuneability of electronic properties and facile synthesis procedure, graphitic carbon nitrides may provide a good balance between activity, durability and cost as materials for polymer electrolyte membrane fuel cells (PEMFCs). We have shown that these materials are promising candidates in PEMFCs as catalyst supports (18,19). Current state-of-the-art technology uses platinum (Pt) or platinum-based alloys supported on carbon black (Vulcan XC-72R) for both anode and cathode electrodes. In order to meet the U.S. Department of Energy (DOE) targets for 2015, it is necessary to reduce the amount of Pt catalyst used by three-quarters while maintaining the same performance and also sufficient durability, which is generally affected by catalyst particle size and dispersion, as well as the interaction between the catalyst particle and the support (20). Therefore, the support plays a crucial role for optimal catalyst performance. The commonly used Vulcan XC-72R is electrochemically unstable at high potential, leading to corrosion after extended operation in acidic media. As the carbon corrodes, Pt nanoparticles agglomerate into larger particles and / or detach from the support material, consequently reducing the electrochemical surface area (ECSA) and catalytic activity (21,22). Much effort has been geared towards the development of alternative, chemically stable catalyst supports. In recent years, numerous conductive ceramics or oxide-containing composites have been studied, including ITO, WO_3, TiO_2, CeO_2 and CeO_2–ZrO_2, WC, Ti_4O_7, NbO_2 or Nb_2O_5, TiN, TiB_2 and SiC (23-33). Various graphitized carbon support materials with special pore structures have also been explored, such as carbon nanotubes (CNT), nanofibers (CNF), nanohorns (CNH) and nanocoils, all showing promising results, although the costly and complex synthesis methods employed constitute a barrier to their introduction into market (34-40). The introduction of nitrogen into carbon supports has showed to improve durability, as well as enhancing the intrinsic catalytic activity for both oxygen reduction (ORR) and methanol oxidation (MOR) reactions (41-48). The N-dopant has been reported to alter the catalyst electronic structure, resulting in a higher binding energy, which may decrease the specific interaction between the Pt nanoparticles and potential poisoning intermediates (49).

Among the different ways to produce high-purity hydrogen, proton-exchange water electrolysis constitutes a promising and efficient solution. First developed by General Electric Co. in 1966 for space applications (50), proton-exchange water electrolyzers (PEMWEs) have been used only for a few large-scale applications. Poor anode kinetics, challenging membrane electrode assembly (MEA) preparation and the need for expensive noble metal catalysts and titanium current collectors have hindered the development of this technology. IrO_2 is the most commonly used anode catalyst due to the superior electrochemical stability and activity for the oxygen evolution reaction (OER). However, iridium is one of rarest elements in the Earth's crust. This inevitably increases the cost of the technology and delays its introduction to the market. Most of the approaches have concentrated on combining IrO_2 with lower-cost materials such as SnO_2 (51),Ta_2O_5 (52), Nb_2O_5 (53), etc. Other approaches recently investigated include replacing Pt by TM carbides such as WC, W_2C and Mo_2C (54). It is thought that mainly by diluting the noble metal content, the metal oxide contributes to the stability of the noble metal particles against degradation. However, the actual processes involved are still not completely clear. The development and use of catalyst support materials in PMWEs remains a considerable challenge due to the highly corrosive reaction environment. The identification and development of less expensive, more efficient and durable anode electrocatalysts is thus vital for the success of PEMWE technology.

To the best of our knowledge, the first application of a gCNM as a catalyst support in energy conversion technologies can be attributed to Yu et al. in 2007 for direct methanol fuel cells (DMFCs) (55). It was shown that PtRu catalyst supported on gCNM in DMFC exhibits 78-83% higher power density than on Vulcan XC-72. However, there have been no further studies to explore the durability and intrinsic catalytic capacity of this system. Here we study the application of different gCNMs as catalyst support in PEMFCs and PEMWEs and investigate their durability and performance in comparison to conventional carbon black, Vulcan XC-72.

Experimental

Synthesis of Graphitic Carbon Nitride Materials

gCNM. This graphitic or polymeric carbon nitride was prepared by thermolysis and condensation reactions of 1:1 molar ratio mixtures of dicyandiamide ($C_2N_4H_4$) and melamine ($C_3N_6H_9$) at 550 ºC. The finely ground starting mixture was loaded in an alumina boat into a quartz tube in a tube furnace under a flow of nitrogen. The temperature was raised at 5 ˚C min^{-1} and held for 15 h. The furnace was allowed to cool to room temperature before the product was removed. Further details of the synthesis and characterization of this material are given elsewhere (17).

PTI/Li^+Cl^-. Poly(triazine) imide carbon nitride (PTI-Li^+Cl^-) was prepared using an ionothermal route (56,57). In a typical synthesis, DCDA was mixed with a eutectic mixture of LiCl/KCl (45:55 wt%) and heated at 400 ^oC for 6h under N_2 (g) followed by a thermal treatment under high vacuum at 600 ^oC for 12h.

B-gCNM. 1-Butyl-3-methylimidazolium tetrafluoroborate ($BminBF_4$) ionic liquid was used to modify the electronic structure of gCNM by substituting C by B (58). $BminBF_4$ also acted as a surfactant increasing the porosity of the material. Adequate amounts to obtain 10 wt% doping were mixed with DCDA and heated in air at 600 ^oC. The brown solid was washed several times with ethanol and dried overnight.

Synthesis of IrO_2 Nanoparticles

IrO_2 was synthesised using the Adams fusion method first described by R. Adams *et al.* (59). This method involves the fusion of the metal chloride precursor $(NH_4)_2IrCl_4$ with $NaNO_3$ in air at elevated temperature. A predetermined amount of $(NH_4)_2IrCl_4$ was dissolved in isopropanol to achieve a metal concentration of $4x10^{-2}$ M, and magnetically stirred for 2 h. An excess of finely ground $NaNO_3$ was added to the solution, which was further stirred for 1 h. The mixture was thermally treated at 500 ^oC for 1 h in air. The obtained black powder was then washed several times with boiling deionised water to remove the unreacted $NaNO_3$. The IrO_2 powder was dried at 80 ^oC overnight.

Preparation of IrO_2-Graphitic Carbon Nitride Mixtures

IrO_2 supported materials were prepared by ball milling IrO_2 nanoparticles and gCNM together in isopropyl alcohol for 6 h at 600 rpm. The resulting paste obtained was dried until a homogeneous powder was obtained. A pre-treatment of gCNM in 5 M HCl helped to protonate the gCNM surface, increasing its polarity and therefore easing the attachment of the IrO_2 nanoparticles to the gCNM surface.

MEA preparation for PEMWE cell

Nafion 115 (thickness ~127 µm, DuPont, USA) was used as the proton exchange membrane for MEA preparation. Before use, the membrane was pretreated in hydrogen peroxide (5 wt%) at 80 ^oC for approximately 1 h to remove organic impurities; after being flushed with deionized water, it was transferred into a 0.5 M sulfuric acid solution at boiled at 80 ^oC for an additional 1 h to protonate the membrane. Finally, the membranes are washed with deionized water. The catalyst inks were prepared by dispersing catalyst powder into a mixture of water and Nafion solution 10% (Sigma Aldrich) and ultrasonically dispersed for 2 h before being used. All MEAs used in this study were prepared by spraying the catalyst ink onto the Nafion membrane using an air-driven spray gun. Catalyst loading for the cathode was 4 mg cm^{-2} of Pt. Catalyst loading for the anode was 1.2 mg cm^{-2} both for the unsupported IrO_2 (IrO_2-No Support) and IrO_2 (40%)-gCNM. The active area of the prepared MEAs was 7.07 cm^{-2}.

Deposition of Pt Catalyst on Graphitic Carbon Nitride

The Pt catalyst was deposited onto gCNM using the ethylene glycol reduction method. Chloroplatinic acid ($H_2PtCl_6;(H_2O)_6$, 0.06 g, Sigma Aldrich) and gCNM (0.09 g) were dispersed in 200 mL of ethylene glycol (Sigma Aldrich). The mixture was stirred for 4 h under nitrogen and then heated to 140°C for 3 h, resulting in a brown-black mixture. The solid product was collected via vacuum filtration and dried at 60°C in a vacuum oven. The Pt loading was 40 wt % to allow comparison with a commercial Pt/Vulcan catalyst formulation (40 wt%, Alfa Aesar).

Structural and Compositional Characterization of Support and Catalysts

C, N, H analyses for gCNMs were performed using a Carlo-Erba EA1108 system. SEM images were acquired using a SEM JEOL JSM-6301F field emission imaging system at 5kV acceleration voltage. TEM images were taken using a JEOL JEM2010 instrument operating at 200 kV; samples were prepared by dispersing the particles in methanol and evaporating the suspension drops on carbon-coated copper grids. Powder X-ray diffraction data were obtained using a Stoe STADI-P diffractometer with Cu $K_{\alpha 1}$ radiation in capillary mode.

Electrochemical Performance Evaluation

In the case of the Pt-supported catalysts, the electrochemical measurements were carried out at 25°C using a conventional three-electrode cell connected to an Autolab PGSTAT32 potentiostat / galvanostat. A glassy carbon (GC) electrode with a geometric surface area of 0.1963 cm^2 was used as a working electrode, which was polished with 0.1 µm alumina (Buehler) followed by washing in deionized water before each use. A catalyst ink of 1.4 g L^{-1} was obtained by dispersing the catalyst in a mixture of acetone, isopropanol and Nafion, ultrasonically for 1 hour. The catalyst ink (25 µL) was deposited on the GC, and dried in air at room temperature, resulting in a typical Pt loading of 35 µg cm^{-2}. A Pt mesh was used as the counter electrode and a hydrogen reference electrode (Gaskatel) was immersed into the Luggin capillary of the electrochemical cell. All potential values mentioned in this work refer to the reversible hydrogen electrode (RHE). The working electrode was electrochemically cleaned prior to each measurement via potential cycling between 0 to 1.2 V for 10 cycles, or until a steady state was reached, at a scan rate of 20 mV s^{-1}, in 0.1 M $HClO_4$ (70% VWR Prolabo Normatom). Cyclic voltammetry (CV) was recorded in the same solution for electrochemical surface area (ECSA) determination. All chemicals used were analytical grade and solutions were prepared with deionised water (18.2 MΩ cm, Millipore). The electrolyte was thoroughly purged with N_2 for 30 minutes prior to every experiment and continuously during the experiment.

The carbon corrosion test used in this work corresponds to a simulation of the start-up / shut-down transients in an operating fuel cell using an accelerated start-stop cycling protocol. The potential was held at 1.0 V for 30 seconds followed by potential cycling between 1.0 V – 1.5 V at 0.5 V s^{-1}. The stability of the support and catalyzed support was evaluated by monitoring the change in the CV profile after cycles 1, 10, 20, 50, 100, 200, 500, 1000 and 2000. The tests were conducted at 60°C in N_2 purged 0.1 M $HClO_4$.

A PEMWE cell supplied by ITM-Power was used to investigate the electrochemical performance of the prepared PEMWE MEAs at 80 ^{o}C. Preheated deionized water (18.3 MΩ cm), which was circulated by two peristaltic pumps at a flow rate of 150 ml min^{-1}, was supplied to both anode and cathode. Polarization curves were recorded galvanostatically between 0 and 0.5 A cm^{-2} at a 0.001 A s^{-1} scan rate. Electrochemical impedance spectroscopy (EIS) measurements were carried out at 0.5 A cm^{-2} with an amplitude of 5 mV in the frequency range of 10 mHz to 10kHz. All electrochemical measurements were performed using an Autolab PGSTAT 30 Potentiostat / Galvanostat equipped with a frequency response analyzer (FRA).

Results and Discussions

Characterization of gCNM supports.

gCNM. Upon heating, the condensation of DCDA and melamine mixture takes place by removal of NH_3 species (3). Elemental analysis revealed that the material had a composition of $C_{3.0}N_{5.2}H_{1.6}$.

A typical X-ray diffraction pattern is displayed in Figure 2a. The strong peak at around 27.5° 2θ corresponds to a repeat distance ~0.323 nm that correlates approximately with the 002 reflection of known graphitic layered materials. The broad feature at around 12.5° 2θ corresponds to an in-plane repeat distance of 0.701 nm. This agrees well with the dimension of a tri-*s*-triazine unit (0.713 nm) found in both polytriazine imide (PTI) and polyheptazine (PH) type structures, and it can be associated with formation of condensed polymeric structures within the layers. Scanning electron microscopy (SEM) examination (Figure 2b) indicated that gCNM exhibits a latticework of interlocking planar microstructures with individual layer thicknesses on the order of 2-3 nm that give rise to porous aggregates with pore sizes on the order of a few nm. This material is not very highly condensed, and its structure could be close to that of Liebig's melon or melem that are built from "ribbons" of PH polymeric units (56,60,61), but with the possibility that PTI units may also be contained within the structure derived from the melamine precursor. The aggregates are fused together to give rise to much larger pores (1-2 μm) within the resulting solid. BET measurements revealed a surface area of 28 m^2 g^{-1}.

PTI-Li^+Cl^-. Poly(triazine) imide carbon nitride (PTI-Li^+Cl^-) was prepared using an ionothermal route (56,57). This method allowed us to obtain a highly crystalline carbon nitride using relatively mild conditions. The PTI-Li^+Cl^- compound exhibits a sharp series of peaks in the X-ray diffraction pattern consistent with a $P6_3cm$ unit cell (Figure 2c). The hexagonal symmetry of the material can be clearly seen in the SEM images that show hexagonal-shaped crystallites (Figure 2d). The material is a polytriazine imide-linked structure $(C_3N_3)_2(NH)_3.LiCl$ (Li: 4.6 %, Cl: 11.0 %) with Li^+ and Cl^- ions intercalated within and between the graphitic layers (56).

B-gCNM. 1-Butyl-3-methylimidazolium tetrafluoroborate ($BminBF_4$) ionic liquid was used to modify the electronic structure of gCNM by substituting C with B. $BminBF_4$ acts also as soft–template inducing higher porosity in the material (62). The X-ray diffraction pattern (Figure 2e) is dominated by the (002) interlayer-stacking reflection usually observed in gCNMs, and the in-plane repeat distance near 0.70 nm is clearly observed. A homogenous porosity with pores of about 50-75 nm was detected by SEM analysis (Figure 2f).

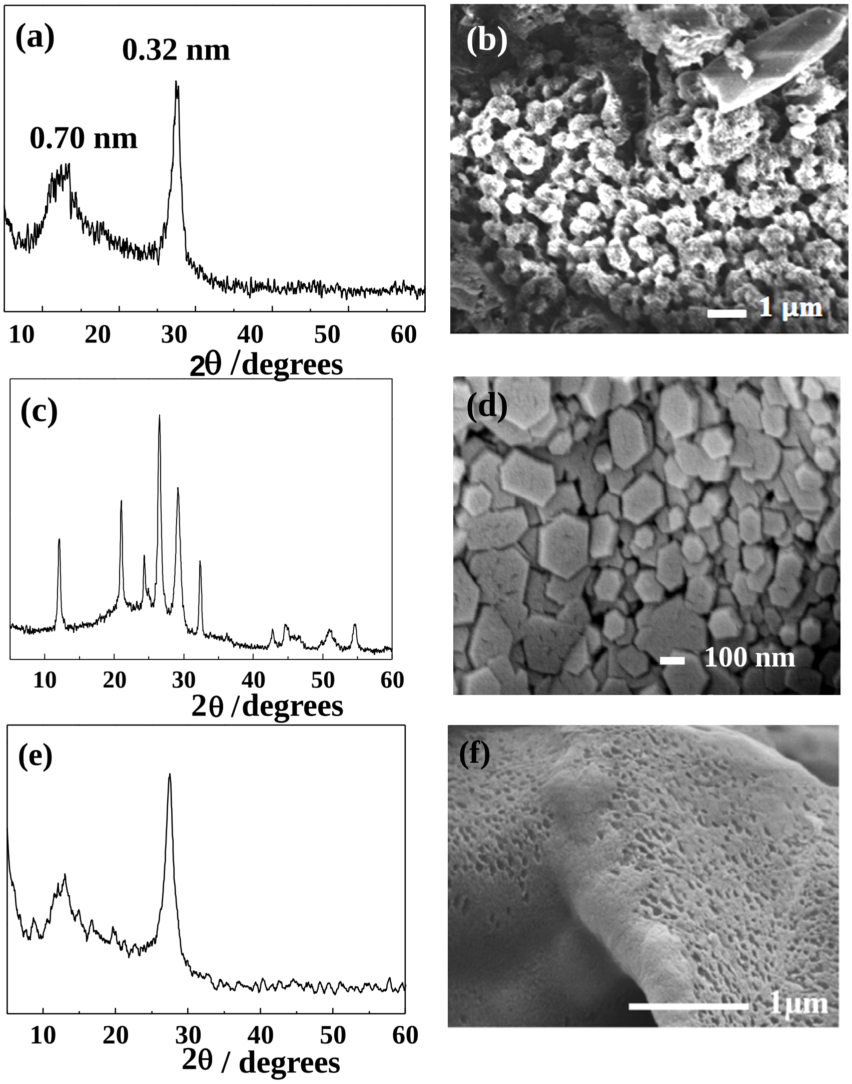

Figure 2. X-ray diffraction pattern and SEM image of (a, b) gCNM, (c, d) PTI-Li^+Cl^-; and (e, f) B-gCNM.

Characterization of supported catalysts.

PEMFCs. Platinum was deposited onto the supports via the ethylene glycol method (63). The materials were characterized via XRD and transmission electron microscopy. The XRD patterns (Figure 3a-d) confirm the presence of platinum in all the samples as characterized by the peaks at 39.8° *2θ* and 46.5° *2θ* corresponding to Pt (111) and (200) reflections, respectively.

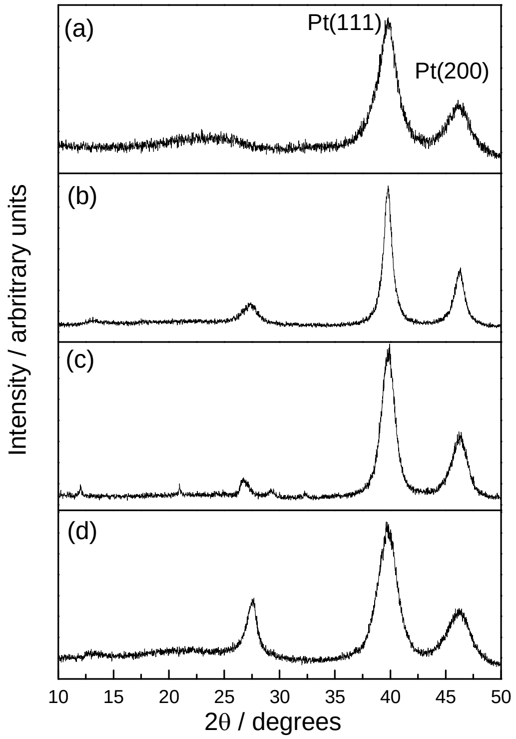

Figure 3. X-Ray diffraction pattern of supported Pt electrocatalysts: (a) Pt/Vulcan (b) Pt/gCNM (c) Pt/PTI-Li^+Cl^- and (d) Pt/B-gCNM.

The TEM images shown in Figure 4a-d indicated varying extents of Pt nanoparticle dispersion in each sample. The average Pt crystallite sizes calculated using the Scherrer equation and also estimated directly from TEM images are shown in Table 1. All Pt on graphitic carbon nitride materials have larger particle sizes (4.2−8.0 nm) compared to commercial Pt/Vulcan (3.5 nm). This is due to the agglomeration in all the samples, indicating that the method used for catalyst deposition for these materials still needs to be optimized.

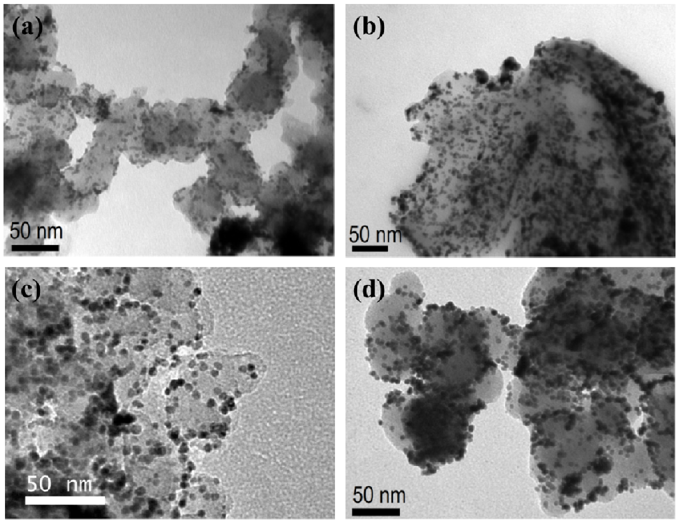

Figure 4. TEM images of (a) Pt/Vulcan (b) Pt/gCNM (c) Pt/PTI-Li^+Cl^- and (d) Pt/B-gCNM.

Table 1. Average Particle and Crystallite Size of Supported Pt Catalysts

	Particle size[a] (nm)	**Crystallite size[b] (nm)**
Pt/Vulcan	3.5	3.6
Pt/gCNM	8.0	8.9
Pt/PTI-Li^+Cl^{l-}	6.4	5.8
Pt/B-gCNM	4.2	3.3

[a]Estimated from TEM images based on the average of 100 particles. [b]Calculated from 111 signal widths of XRD using the Scherrer equation.

PEMWEs. IrO_2 nanoparticles were synthesized by the Adam's fusion method.(59) Prior to depositing IrO_2 onto gCNM, gCNM prepared by thermolysis of 1:1 molar ratio DCDA and melamine at 550 ^oC in N_2 (g), was treated in 5M HCl to help IrO_2 nanoparticles to attach to its surface. Adequate amounts of IrO_2 and gCNM to achieve 40 wt% IrO_2 were mixed using ball-milling method at 600 rpm for 6h in isopropyl alcohol. This method allowed a better nanoparticle distribution compared to conventional grinding. Figure 5 shows the HRTEM images of IrO_2 and IrO_2 (40%)-gCNM. As can be observed, the ball-milling treatment decreased the particle size of IrO_2 from ~15 nm to ~5 nm, contributing to increase the active surface area of the catalyst and to improve its distribution on the gCNM support.

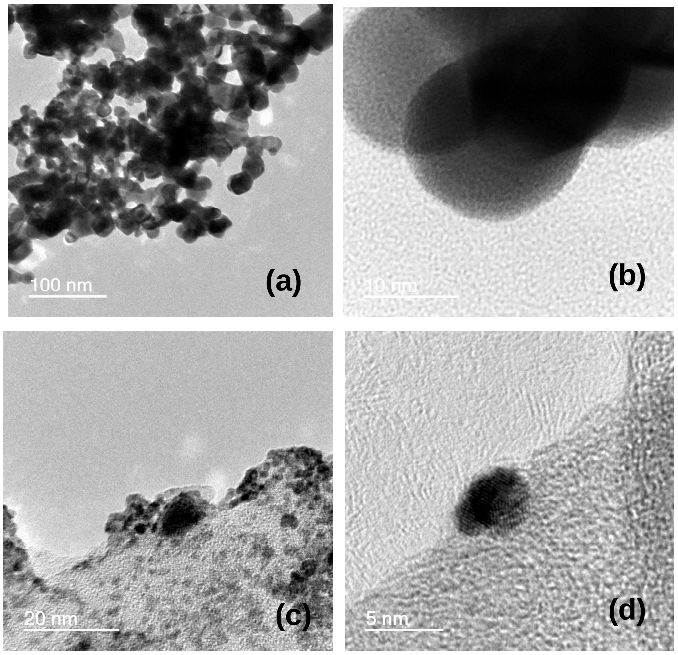

Figure 5. HRTEM images of (a, b) IrO_2 nanoparticles; (c, d) IrO_2 (40)-gCNM.

Electrochemical Characterization.

Durability of support. The stability of the carbon nitrides was determined by observing the change in double-layer capacitance in the cyclic voltammetry (CV) measurements while performing the carbon corrosion test (Figure 6a). The capacitance was calculated at

0.40 V and normalised to the 10th scan. Capacitance increases with the number of scans due to an increase in surface area and concentration of hydrophilic carbon corrosion products with oxygen functionalities at the surface of the carbon support (64,65). The presence of oxygenated species reduces the durability of PEFC catalysts by promoting carbon corrosion (66). In addition, a more hydrophilic surface may affect water management in fuel cells and potentially contribute to performance instability and variability. Figure 6a displays the degree of corrosion behavior/surface modification of gCNM compared with the commercial Vulcan carbon support. After approximately 500 cycles, the carbon nitride materials clearly exhibited a higher degree of tolerance to degradation relative to Vulcan, with B-gCNM showing the best performance with only a 6 % increase in capacitance at the end of the cycle.

The durability of the materials in the presence of Pt nanoparticles was evaluated using the same accelerated protocol, with CV and electrochemical surface area (ECSA) recorded at regular intervals as part of the diagnostic. The ECSA was calculated by measuring the hydrogen adsorption/desorption peaks on the CV in terms of the total charge passed during the H^+ adsorption with the assumption that one metal atom adsorbs one hydrogen atom (67). The results are summarized in Table 2. All gCNM supported Pt catalysts have lower initial ECSA compared to the commercial material. This is due to higher degree of agglomeration and larger particle size, as shown in Figure 4. This comparison also indicates that each graphitic carbon nitride material has a different ability to accommodate catalyst particles and allow access to them. The gCNMs studied here have approximately one order of magnitude less BET determined surface area compared to Vulcan carbon, and hence the same mass percentage loading of Pt nanoparticles on Vulcan would correspond to a higher Pt particle density on the carbon nitride supports.

Pt/B-gCNM has a significantly lower initial ECSA compared to Pt/gCNM and Pt/PTI-Li^+Cl^-. This is attributed to the lower degree of particle dispersion and larger particle size, as shown in Figure 4. Pt/PTI-Li^+Cl^- has the highest initial ECSA, twice larger than that for Pt/gCNM. In addition to the small particle size and enhanced particle dispersion, PTI-Li^+Cl^- is more soluble in 70% IPA, owing to the presence of Li^+ and Cl^-, resulting in well-dispersed catalyst ink and better electrode quality.

Table 2. The ECSA of supported Pt electrocatalysts before and after the accelerated carbon corrosion cycling (2000 cycles).

	Initial ECSA (m^2 g^{-1})	**Final ECSA (m^2 g^{-1})**	**ECSA loss (%)**
Pt/Vulcan	28.6	18.2	36.3
Pt/gCNM	7.2	1.8	81.0
Pt/PTI-Li^+Cl^-	15.9	12.8	19.3
Pt/B-gCNM	1.9	0	100

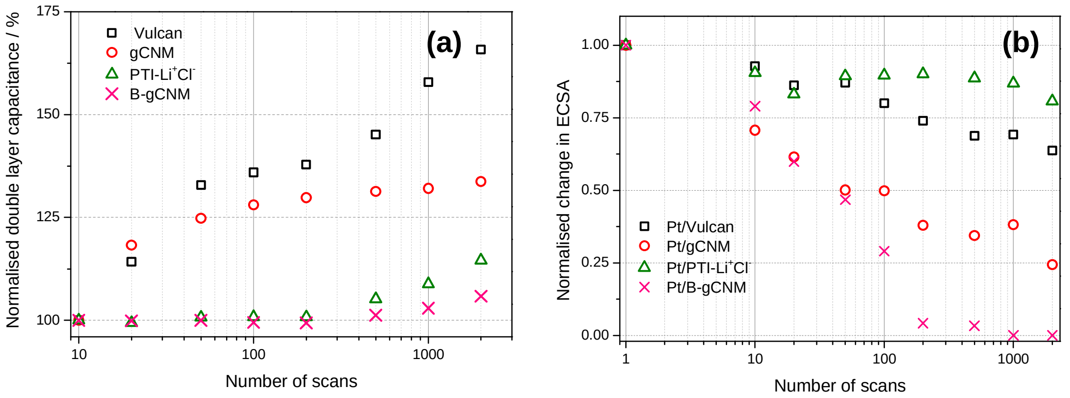

Figure 6. (a) The change in double-layer capacitance (calculated at 0.40 V) of the support materials as a result of accelerated carbon corrosion cycling; (b) The change in ECSA (calculated from hydrogen adsorption/desorption) of the supported Pt electrocatalsysts as a result of accelerated carbon corrosion cycling.

Figure 6b. The decrease in ECSA is believed to be due to platinum agglomeration and dissolution as a result of substrate corrosion (68). As the substrate undergoes corrosion, Pt nanoparticles will start agglomerating which will lead to their detachment from the support and consequently decrease in ECSA. At the end of the 2000 cycles, commercial Pt/Vulcan exhibits a 36.3% decrease in ECSA (Table 2). Pt/gCNM and Pt/B-gCNM show higher ECSA loss at 81.0% and 100% loss respectively, despite each support having higher degree of corrosion tolerance, as displayed on Figure 6a Pt/PTI-Li$^+$Cl$^-$ exhibits the highest durability at only 19.3% ECSA loss. In addition, it is also observed that graphitic carbon nitride supported Pt catalysts with higher initial ECSA exhibit higher electrochemical durability, indicating there is a link between good metal-support interaction and durability. Support material that provides strong adsorption and anchoring sites for the Pt nanoparticles will increase particle dispersion and limit leaching and agglomeration processes during the accelerated test (69).

Electrocatalytic activity. The catalytic activities of graphitic carbon nitride supported Pt catalysts were investigated in 1 M methanol + 0.1 M $HClO_4$ solution at 25^{o}C. Figure 7 compares the methanol oxidation peak of each supported catalyst. It is generally accepted that low overpotential and high peak current density is an indication of good methanol oxidation reaction (MOR) activity. The current density is normalized to the ECSA of each respective material. The results are summarized on Table 3 All gCNM supported catalysts exhibit lower overpotential and higher peak current density compared to Pt/Vulcan. Pt/PTI-Li$^+$Cl$^-$ exhibits the lowest overpotential whereas Pt/B-gCNM has the highest peak current density. The MOR overpotential is expected to be influenced by particle size effects: smaller Pt nanoparticles enhance the oxidation of poisoning intermediates and hence, decrease the overpotential. Given particle size is similar in both Pt/Vulcan and Pt supported on carbon nitrides, particle size effect can be eliminated from this observation. This suggests that the presence of nitrogen on/within the support material could lead to intrinsic MOR catalytic enhancement. However, more work is needed to optimize the particle dispersion and ECSA.

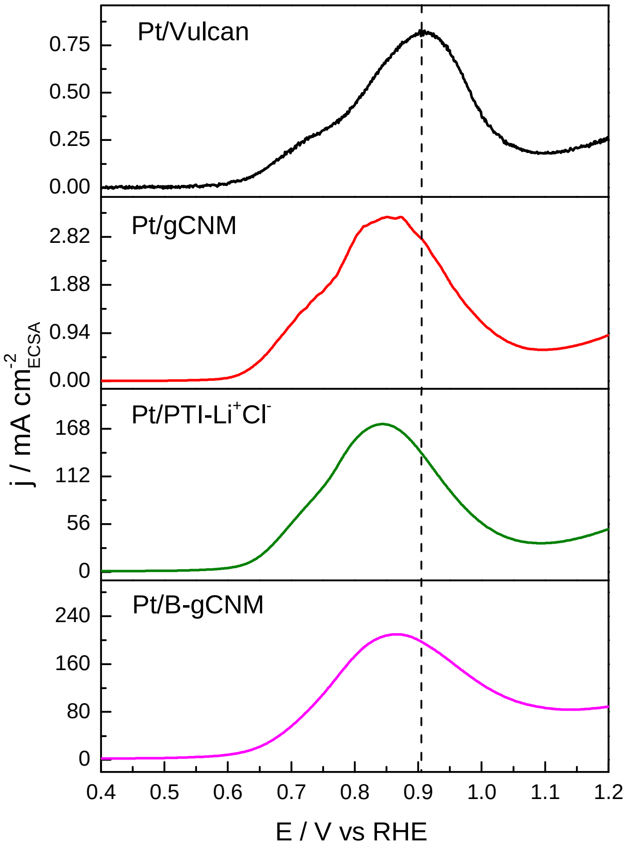

Figure 7. Methanol oxidation reaction of supported Pt electrocatalysts in 1 M CH_3OH + 0.1 M $HClO_4$ at 25°C with a scan rate of 2 mV s^{-1}.

Table 3. The methanol oxidation peak potential (E_{peak}) and maximum methanol oxidation reaction current density (j_{max}) of supported Pt electrocatalysts in 1 M CH_3OH + 0.1 M $HClO_4$ at 25°C.

	E_{peak} [V]	**j_{max} [mA $cm^{-2}{}_{ECSA}$]**
Pt/Vulcan	0.903	0.821
Pt/gCNM	0.850	3.21
Pt/PTI-Li^+Cl^-	0.842	174
Pt/B-gCNM	0.858	209

Electrochemical performance of IrO_2 (40%)-gCNM for PEMWEs. Figure 8 shows the polarization curves obtained for the PEMWE tested with unsupported IrO_2 (IrO_2-No Support) and IrO_2 supported on gCNM (IrO_2(40%)-gCNM). The loading of metal in both cases was 1.2 mg cm^{-2}. Open circuit voltage (OCV) values of 1.49 and 1.53 V, respectively, were obtained in each case. The PEMWE cell achieved a potential of 1.85 V and 2.30 V at 0.42 A cm^{-2} when polarized with the unsupported vs supported IrO_2 catalysts, respectively, indicating that the IrO_2(40%)-gCNM material has poorer performance. However, improvement in nanoparticle dispersion techniques combined with an increase in porosity of the gCNM is expected to improve the voltage response at high current densities.

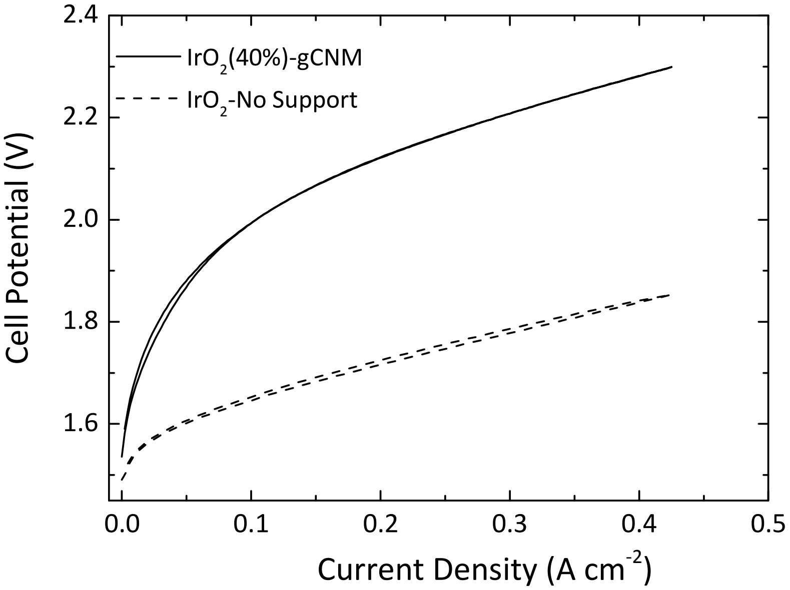

Figure 8. VI measurements of the PEM water electrolyzer operating at 80 °C and ambient pressure, 1 atm.

Nyquist plots obtained for the PEM electrolyzer cell with IrO_2-No Support and IrO_2(40%)-gCNM at current densities of 0.14 and 0.28 A cm^{-2} are shown in Figure 9a. The plots were fitted with an equivalent circuit shown in Figure 9b containing a resistor in series with an RC parallel combination. R_{el} is attributed to the purely ohmic resistance of the cell determined by the Nafion membrane and current collectors. R_{ct} (charge transfer resistance) represents the kinetics of the anode assuming that those of the cathode are insignificant due to fast hydrogen evolution kinetics. Distortion of capacitance due to nonuniformity and roughness of the electrode can be correlated with the constant phase element, CPE, for $n = 1\text{-}\varepsilon$, where $0<\varepsilon\leq 0.2$. R_{ct} can be determined by the difference between the low and high frequency intercepts on the real axis.

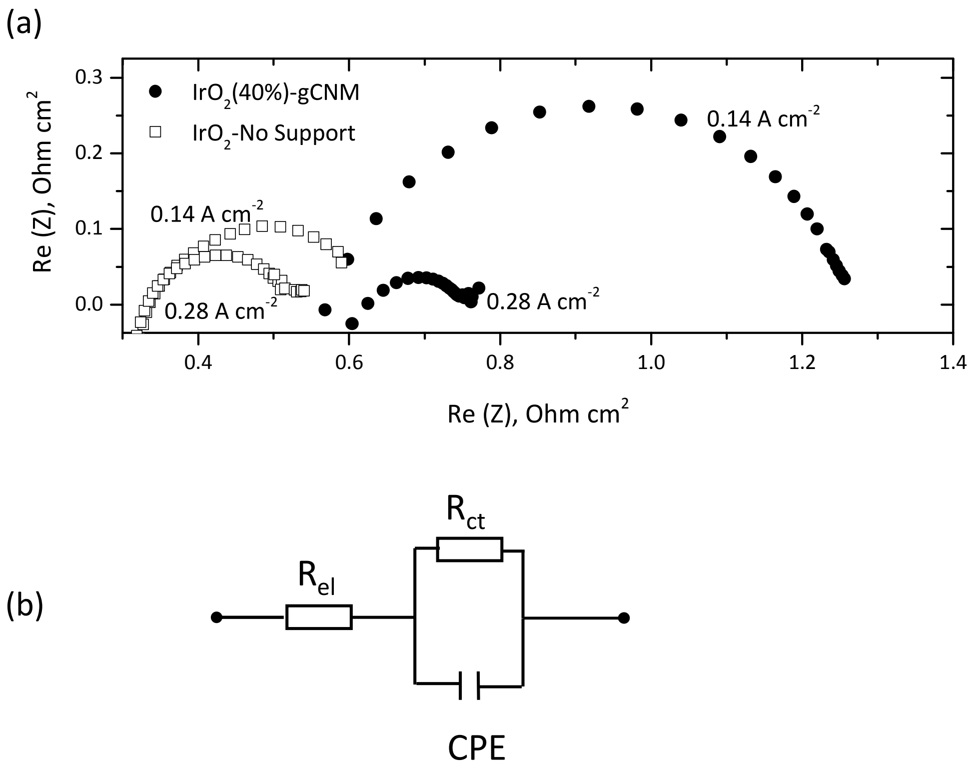

Figure 9(a): Nyquist plots of a PEM water electrolyzer tested with IrO_2(40%)-gCNM and IrO_2(40%)-No Supported as anode electrocatalysts operating at 80 °C, ambient pressure. (b) Equivalent circuit for the electrolysis cell indicating ohmic and charge transfer resistances.

The fitted parameters tabulated in Table 3 indicate that R_{el} at 0.14 A cm^{-2} has values of 0.32 and 0.55 Ω cm^2 for unsupported IrO_2 and gCNM supported IrO_2, indicating that gCNM has a negative effect on the ohmic resistance of the cell, which can be associated with its poor conductivity. The difference in R_{el} values of gCNM supported IrO_2 at different current densities can be explained by slight temperature drop (~3-5 ^{o}C) observed during the measurements. Although the presence of gCNM increases the ohmic resistance the R_{ct} data in Table 2 illustrates that use of a gCNM support improves the kinetics of the anode reaction significantly as the current density increases. This effect is visible in Figure 9a as the diameter of the Nyquist plots reduces considerably in the presence of gCNM. R_{ct} reduces from 0.81 to 0.16 Ω cm^2 when the current density is increased from 0.14 to 0.28 A cm^{-2} for gCNM supported IrO_2 and is much lower than that of unsupported IrO_2 at the same current density. The relatively poor conductivity of gCNM would explain the higher ohmic resistance seen in the electrochemical impedance spectra and also the high voltage response observed in the VI curve. However, there is an enhancement in the charge transfer behavior and therefore the kinetics of electrocatalytic activity of the catalyst nanoparticles supported on gCNM.

Conclusions

The results presented in this paper show that graphitic carbon nitrides are promising catalyst supports for PEMFC and PEMWE applications. In the case of PEMFCs, Pt-supported gCNMs exhibited better durability than commercial Vulcan XC-and therefore, are promising catalyst support materials for PEMFC applications. Interestingly, B-gCNM and PTI/Li^+Cl^- exhibit the highest stability, suggesting that crystallinity and presence of dopants may play an important role in the stability of the material against carbon corrosion. The durability of Pt-gCNM electrocatalysts is highly dependent on the initial ECSA. B-gCNM, with the lowest ECSA, exhibits the lowest durability with a loss of 100% after 2000 cycles. The PTI/Li^+Cl^- has the best durability of all Pt-supported catalysts with an ECSA loss of only 19% after 2000 cycles, lower than that of Pt/Vulcan with an ECSA loss of 36% at the same stage. In addition, all graphitic supported Pt electrocatalysts have higher methanol oxidation activity per ECSA, compared to Pt/Vulcan. Preliminary results on IrO_2 supported on gCNM show that gCNM improves the charge transfer kinetics as the current density increases and therefore the electrocatalytic activity of the catalyst nanoparticles.

Table 3 Fitted parameters of EIS data shown in Figure 9a to the equivalent circuit shown in Figure 9b.

Anode	**Current density (A cm^{-2})**	**Metal loading (mg cm^{-2})**	**OCV**	R_{el} **(Ω cm^2)**	R_{ct} **(Ω cm^2)**	**CPE (Ω^{-1}s^n)**	***n***
IrO_2(40%)-gCNM	0.14	1.6	1.53	0.550	0.810	0.006	0.77
IrO_2(40%)-gCNM	0.28	1.6	1.53	0.575	0.160	0.007	0.70
IrO_2-No Support	0.14	1.6	1.49	0.323	0.309	0.233	0.73
IrO_2-No Support	0.28	1.6	1.49	0.312	0.211	0.213	0.65

Acknowledgments

The authors acknowledge the EPSRC and UCL Enterprise Impact Acceleration Account (EP / K503745 / 1) and EPSRC Supergen Fuel Cells (EP / G030995 / 1) and the EPSRC UK Catalysis Hub (EP / K0144706 / 1) for financial support. McMillan and Brett also acknowledge the EPSRC Centre for Nature Inspired Engineering (EP / K038656 / 1).

References

---

1. J. Liebig, *Ann. Pharm.*, **10**, 1 (1834).

2. E. C. Franklin, *J. Am. Chem. Soc.*, **44**, 486 (1922).

3. E. Kroke and M. Schwarz, *Coord. Chem. Rev.*, **248**, 493 (2004).

4. E. Kroke, M. Schwarz, E. Horath-Bordon, P. Kroll, B. Noll and A. D. Norman, *New J. Chem.*, **26**, 508 (2002).

5. T. Komatsu, *J. Mater. Chem.*, **11**, 802 (2001).

6. G. Demazeu, H. Montigaud, B. Tanguy, M. Birot and J. Dunogues, *Rev. High Pressure Sci. Technol.*, **7**, 1345 (1998).

7. G. Goglio, D. Andrault, S. Courjault, G. Demazeau, *High Pressure Res.*, **22**, 535 (2002).

8. G. Goglio, D. Foy and G. Demazeau, *Mater. Sci. Eng. R. Rep.*, **58**, 195 (2008).

9. S. W. Kohl, L. Weiner, L. Schwartsburd, L. Konstantinovski, L. J. W. Shimon, Y. Ben-David, M. A. Iron and D. Milstein, *Science*, **324**, 74 (2009).

10. H. Liu, T. Jiang, B. Han, S. Liang and Y. Zhou, *Science*, **326**, 1250 (2009).

11. F. Su, S. C. Mathew, G. Lipner, X. Fu, M. Antonietti, S. Blechert and X. Wang, *J. Am. Chem. Soc.*, **132**, 16299 (2010).

12. X. Wang, K. Maeda, A. Thomas, K. Takanabe, G. Xin, J. M. Carlsson, K. Domen and M. Antonietti, *Nat Mater*, **8**, 76 (2009).

13. Y. Wang, Y. Di, M. Antonietti, H. Li, X. Chen and X. Wang, *Chem. Mater.*, **22**, 5119 (2010).

14. Y. Wang, X. Wang and M. Antonietti, *Angew. Chem. Int. Ed.*, **51**, 68 (2012).

15. F. Z. Su, S. C. Mathew, G. Lipner, X. Z. Fu, M. Antonietti, M. S. Blechert and X. C. Wang, *J. Am. Chem. Soc.*, **132**, 1629 (2010).

16. Y. Wang, J. Zhang, X. Wang, M. Antonietti and H. Li, *Angew. Chem. Int. Ed.*, **49**, 3356 (2010).

(17) A. Belen Jorge, D. J. Martin, M. T. S. Dhanoa, A. S. Rahman, N. Makwana, J. Tang, A. Sella, F. Corà, S. Firth, J. A. Darr, and P. F. McMillan, *J. Phys. Chem. C*, **117**, 7178 (2013).

18. N. Mansor, A. Belen Jorge, F. Corà, C. Gibbs, R. Jervis, P. F. McMillan, X. Wang and D. J. L. Brett, *J. Phys. Chem. C.*, **118**, 6831 (2014).

19. N. Mansor, A. Belen Jorge, F. Corà, C. Gibbs, R. Jervis, P. F. McMillan, X. Wang and D. J. L. Brett, *ECS Trans*, **58**, 1767 (2013).

20. U. S. Department of Energy. Fuel Cell Technologies Office Multi-Year Research, Development and Demonstration Plan, http://www1.eere.energy.gov/hydrogenandfuelcells/mypp/ (2012).

21. Y. Shao, G. Yin, Z. Wang and Y. Gao. *J. Power Sources*, **437**, 229 (2007).

22. X. Sun, R. Li, D. Villers, J. P. Dodelet and S. Désilets. *Chem. Phys. Lett.*, **379**, 899 (2003).

23. B. Avasarala, T. Murray, W. Li and P. Haldar, *J. Mater. Chem*, **19**, 1803 (2009).

24. H. Chhina, S. Campbell and O. Kesler, *J. Power Sources*, **161**, 893 (2006).

25. T. Ioroi, Z. Siroma, N. Fujiwara, S.-i. Yamazaki and K. Yasuda, *Electrochem. Comm.*, **7**, 183 (2005).

26. H. Lv, S. Mu, N. Cheng and M. Pan, *Appl. Catal., B: Env*, **100**, 190 (2010).

27. J. Rajeswari, B. Viswanathan and T. K. Varadarajan, *Mater. Chem. Phys.*, **106**, 168 (2007).

28. W. Ruettinger, X. Liu and R. J. Farrauto, *Appl. Catal., B: Env*, **65**, 135 (2006).

29. H. Sakurai, T. Akita, S. Tsubota, M. Kiuchi and M. Haruta, *Appl. Catal., A: General*, **291**, 179 (2005).

30. K. Sasaki, L. Zhang and R. R. Adzic, *Phys. Chem. Chem. Phys.*, **10**, 159 (2008).

31. P. K. Shen, S. Yin, Z. Li and C. Chen, *Electrochim. Acta*, **55**, 7969 (2010).

32. S. von Kraemer, K. Wikander, G. Lindbergh, A. Lundblad and A. E. C. Palmqvist, *J. Power Sources*, **180**, 185 (2008).

33. S. Yin, S. Mu, M. Pan and Z. Fu, *J. Power Sources*, **196**, 7931 (2011).

34. E. Antolini, *Appl. Catal., B: Env*, **88**, 1 (2009).

35. D. He, S. Mu and M. Pan, *Carbon*, **49**, 82 (2011).

36. T. Hyeon, S. Han, Y.-E. Sung, K.-W. Park and Y.-W. Kim, *Angew. Chem. Int. Ed.*, **42**, 4352 (2003).

37. M. Sevilla, G. Lota and A. B. Fuertes, *J. Power Sources*, **171**, 546 (2007).

38. G. G. Wildgoose, C. E. Banks and R. G. Compton, *Small*, **2**, 182 (2006).

39. T. Yoshitake, Y. Shimakawa, S. Kuroshima, H. Kimura, T. Ichihashi, Y. Kubo, D. Kasuya, K. Takahashi, F. Kokai, M. Yudasaka and S. Iijima, *Physica B: Condens. Mater.*, **323**, 124 (2002).

40. S. Zhang, Y. Shao, G. Yin and Y. Lin, *J. Mater. Chem*, **20**, 2826 (2010).

41. R. Chetty, S. Kundu, W. Xia, M. Bron, W. Schuhmann, V. Chirila, W. Brandl, T. Reinecke and M. Muhler, *Electrochim. Acta*, **54**, 4208 (2009).

42. S. Kundu, T. C. Nagaiah, W. Xia, Y. Wang, S. V. Dommele, J. H. Bitter, M. Santa, G. Grundmeier, M. Bron, W. Schuhmann and M. Muhler, *J. Phys. Chem. C.*, **113**, 14302 (2009).

43. Z. Lei, L. An, L. Dang, M. Zhao, J. Shi, S. Bai and Y. Cao, *Microporous Mesoporous Mater.*, **119**, 30 (2009).

44. J.-i. Ozaki, T. Anahara, N. Kimura and A. Oya, *Carbon*, **44**, 3358 (2006).

45. G. Wu, D. Li, C. Dai, D. Wang and N. Li, *Langmuir*, **24**, 3566 (2008).

46. S. C. Roy, P. A. Christensen, A. Hamnett, K. M. Thomas and V. Trapp, *J. Electrochem. Soc.*, **143**, 3073 (1996).

47. E. Negro, K. Vezzù, F. Bertasi, P. Schiavuta, L. Toniolo, S. Polizzi and V. Di Noto, *ChemElectroChem*, **1**, 1359 (2014).

48. V. Di Noto, E. Negro, S. Polizzi, K. Vezzù, L. Toniolo and G. Cavinato, *Int. J. Hydrogen Energy*, **39**, 2812 (2014).

49. Y. Zhou, R. Pasquarelli, T. Holme, J. Berry, D. Ginley and R. O'Hayre, *J. Mater. Chem*, **19**, 7830 (2009).

---

50. J. H. Russell, L. J. Nuttall, A. P. Fickett. Hydrogen Generation by Solid Polymer Electrolyte Water Electrolysis. American Chemical Society Division of Fuel Chemistry Preprints, 18(3): 24e40 (1973).

51. C. P. De Pauli and S. Trasatti, *J. Electroanal. Chem.*, **396**, 161 (1995).

52. M. Morimitsu, R. Otogawa and M. Matsunaga, *Electrochim. Acta*, **46**, 401 (2000).

53. A. J. Terezo, J. Bisquert, E. C. Pereira and G. Garcia-Belmonte, *J. Electroanal. Chem.*, **508,** 59 (2001).

54. D. V. Esposito, S. T. Hunt, Y. C. Kimmel and J. G. Chen, *J. Am. Chem. Soc.*, **134**, 3025 (2012).

55. M. Kim, S. Hwang and J.-S. Yu, *J. Mater. Chem*, **17** (2007).

56. E. Wirnhier, M Döblinger, D. Gunzelmann, J. Senker, B. V. Lotsch and W. Schnick. *Chem.-Eur. J.*, **17**, 3213 (2011).

57. M. J. Bojdys, J.-O. Müller, M. Antonietti and A. Thomas, *Chem. –Eur. J.*, **14**, 8177 (2008).

58. Y. Zhang, T. Mori, J. Ye and M. Antonietti, *J. Am. Chem. Soc.,* **132**, 6294 (2010).

59. R. Adams, V. Voorhees, and R. L. Shriner, *Org. Synth.*, **8**, 92 (1928).

60. B. V. Lotsch and W. Schnick, *Chem. Mater*., **18**, 1891 (2006).

61. B. Jürgens, E. Irran, J. Senker, P. Kroll, H. Müller and W. Schnick, *J. Am. Chem. Soc.*, **125**, 10288 (2003).

62. Y. Wang, J. Zhang, X. Wang, M. Antonietti and H. Li. *Angew. Chem., Int. Ed.,* **49**, 3356 (2010).

63. D. Larcher and R. Patrice, *J. Solid State Chem.,* **154**, 405 (2000).

64. M. J. Bleda-Martínez, J. A. Macia-Agullo, D. Lozano-Castello, E. Morallon, D. Cazorla-Amoros and A. Linares-Solano, *Carbon*, **43**, 2677 (2005).

65. A. P. Young, J. Stumper, E. Gyenge, *J. Electrochem. Soc.*, **156**, B913 (2009).

66. X. Yu and S. Ye, *J. Power Sources*, **172**, 145 (2007).

67. R. Woods, *J. Electroanal. Chem. Interfacial Electrochem.*, **49**, 217 (1974).

68. J. Zhou, X. Zhou, X. Sun, R. Li, M. Murphy, Z. Ding, X. Sun and T.-K. Sham, *Chem. Phys. Lett.*, **437**, 229 (2007).

69. Y. Zhou, K. Neyerlin, T. S. Olson, S. Pylypenko, J. Bult, H. N. Dinh, T. Gennett, Z. Shao and R. O’Hayre, *Energy Env. Sci.*, **3**, 1437 (2010).